

Gravity-destabilized nonwetting phase invasion in macroheterogeneous porous media: Experimental observations of invasion dynamics and scale analysis

Robert J. Glass, Stephen H. Conrad, and William Peplinski

Flow Visualization and Processes Laboratory, Sandia National Laboratories, Albuquerque, New Mexico

Abstract. We designed and conducted experiments in a heterogeneous sand pack where gravity-destabilized nonwetting phase invasion (CO_2 and trichloroethylene) could be recorded using high-resolution light transmission methods. The heterogeneity structure was designed to be reminiscent of fluvial channel lag cut-and-fill architecture and to contain a series of capillary barriers. As invasion progressed, nonwetting phase structure developed a series of fingers and pools; behind the growing front we found nonwetting phase saturation to pulsate in certain regions when viscous forces were low. Through a scale analysis we derive a series of length scales that describe finger diameter, pool height and width, and regions where pulsation occurs within a heterogeneous porous medium. In all cases we find that the intrinsic pore-scale nature of the invasion process and resulting structure must be incorporated into our analysis to explain experimental results. We propose a simple macroscale structural growth model that assembles length scales for substructures to delineate nonwetting phase migration from a source into a heterogeneous domain. For such a model applied at the field scale for dense nonaqueous phase liquid migration, we expect capillary and gravity forces within the complex subsurface lithology to play the primary roles with viscous forces forming a perturbation on the inviscid phase structure.

1. Introduction

Spilled solvents have created pervasive groundwater contamination problems because of their ubiquitous use, their toxicity and persistence in the environment, and the difficulty of recovering them from the subsurface. Because organic solvents are more dense than water and immiscible with water, they are commonly referred to as DNAPLs (dense nonaqueous phase liquids). They migrate below the water table downward and laterally under the influence of gravity, capillary, and viscous forces. Because DNAPLs are generally the nonwetting fluid, variations in media texture that the DNAPLs encounter as they migrate can have a profound influence on the migration path. This capillary control induced by textural heterogeneities complicates the migration of the DNAPLs and makes it difficult to predict the locations in the aquifer where the spilled DNAPLs may ultimately reside. Uncertainties in the region of solvent contamination translate into higher remediation costs because the remedial system must be designed in light of these uncertainties.

Several experiments have shown the importance of heterogeneous texture in affecting the migration of DNAPLs in two-phase systems in laboratory sand packs [Kueper *et al.*, 1989; Illangasekare *et al.*, 1995, 1996] and in micromodels [Conrad *et al.*, 1989; Wilson *et al.*, 1990]. Similarly, two-dimensional (2-D), heterogeneous, glass bead pack experiments have been performed for the upward migration of a gas [Ji *et al.*, 1993], also the nonwetting fluid. Additionally, two field experiments of DNAPL migration below the water table have been conducted

at the Borden site [Kueper *et al.*, 1993; Brewster *et al.*, 1995]. Not surprisingly, all these studies have produced irregular spatial distributions of the nonwetting phase. Experimental and modeling studies of DNAPL dissolution processes in heterogeneous systems [e.g., Anderson *et al.*, 1992; Powers *et al.*, 1998] have shown that this irregular distribution of DNAPLs has significant impacts on the rate of dissolution. Of course, it also has implications for remedial strategies that attempt to improve pump and treat by enhancing dissolution, for example, surfactants or cosolvents, or oxidizing the DNAPL in situ, for example, potassium permanganate.

The complicated pattern and dependence on small-scale detail places nonwetting invasion in a separate class from wetting invasion where combinations of film flow and multiple neck pore filling facilitation create macroscopic fronts [e.g., Lenormand and Zarcone, 1985; Blunt and Scher, 1995; Glass and Yarrington, 1996]. Modeling nonwetting displacements with current two-phase continuum-scale porous media approaches that integrate over a large number of pores in an effort to define effective behavior at a representative elementary volume (REV) scale must be considered as questionable for many situations. Alternative modeling approaches that better embody the underlying physics make use of modified forms of invasion percolation (MIP). While forms of MIP have been applied in the past to yield phenomenological understanding in small random pore networks, our desire is to develop such models to be predictive of system behavior at much larger scales [e.g., Kueper and McWhorter, 1992; Glass *et al.*, 1995; Ioannidis *et al.*, 1996; Ewing and Berkowitz, 1998]. While still in their infancy, such approaches show great promise. In order to develop these models as well as to test current porous continuum approaches, experiments are required that capture inva-

This paper is not subject to U.S. copyright. Published in 2000 by the American Geophysical Union.

Paper number 2000WR900152.

sion dynamics within large heterogeneous pore networks under the combined influence of capillary, gravity, and viscous forces.

In this paper we present and analyze three experiments designed to quantitatively visualize the evolving invasion structure during gravity-destabilized, nonwetting phase invasion within macroheterogeneous porous media. We built our media to create a series of capillary barriers and evoke lithology reminiscent of fluvial channel lag cut-and-fill architecture within translucent sands. Using light transmission techniques, we collected invasion data rapidly at near pore-scale resolution. These data allow us to track the invasion front with exceptional clarity and analyze the unsteady dynamics of the phase invasion process both during initial invasion and upon redistribution. Our experiments demonstrate a characteristic alternation between gravity-stabilized and gravity-destabilized invasion growth controlled by the sequential capillary barriers within the heterogeneous field. Under gravity-destabilized growth periods, pore-scale fingering is organized away from the source, while under gravity-stabilized periods, invasion coalesces into macroscopic horizontal fronts that grow backward, overwriting the original finger structure. Behind the invasion front we find rich dynamics with multiple cycle pulsation before, within, and beyond capillary barriers and along the path of fingers, yielding highly nonmonotonic saturation behavior in time and space.

Through a scale analysis using local force balances, we derive a series of length scales that control invasion structure and dynamics such as finger diameter, the height of pools above capillary barriers, and the location of zones of nonwetting fluid pulsation. In all cases we find that the intrinsic pore-scale nature of the invasion process and resulting structure must be incorporated into our analysis to explain experimental results. Analysis also demonstrates that while global viscous forces are small, the pore-scale nature of capillary barrier breaching and fingering can cause them to be locally significant and of the order of capillary and gravity forces. Such results suggest significant difficulties in the application of standard porous continuum approaches. We propose an alternative modeling approach that assembles these length scales within the context of a macroscale “structural” growth model akin to upscaled MIP. Such a model yields directly the nonwetting phase migration pathway evolution, its geometry of fingers and pools, and the locations of zones of pulsation within complex subsurface lithologic heterogeneity. Inadequacies of continuum-scale models can thus be avoided, and the structural growth model can be combined easily with high-resolution Monte Carlo simulation of the controlling subsurface geology to yield probabilistic prediction of subsurface DNAPL contamination.

2. Experimental Design

We designed experiments within a thin but extensive sand chamber where we could use quantitative light transmission techniques to record invasion dynamics in time. A reproducible heterogeneity structure was placed within the chamber, and three constant-flux, gravity-destabilized, nonwetting phase invasion experiments were conducted where we varied the interfacial tension, density difference, and viscosity using two fluid-fluid systems: CO₂-water and trichloroethylene (TCE)-water.

2.1. Chamber Construction

The chamber was constructed of two plates of hydrophilic glass (1.25 cm thick) held apart by two aluminum spacers (1 cm

thick) that ran down the long edges of the glass. The internal dimensions of the chamber were 1 cm thick (~10–40 pores/grains) by 26 cm wide by 60 cm tall. O rings embedded in the edge spacers provided a seal with forces applied by an external clamp that ran the length of the chamber sides. At the top and bottom a screened manifold and a porous plate, respectively, were sealed to the chamber allowing for the inflow and outflow of water. Steel bars were clamped to the outside of the glass plates at the top and bottom to minimize chamber bowing under the pressures created by filling the chamber with sand and fluids. A port for injecting the nonwetting phase was laterally centered in the front glass plate, within 3 cm of one edge.

2.2. Sand Packing

The chamber was filled using a sand filler designed to create reproducible “facies-like” geometric structures. A computer-controlled positioner was mounted on a platform, which could be raised and lowered manually. Attached to the positioner was a sand hopper, funnel, tube, and vibration source that delivered sand to the chamber at specified locations. Horizontal position, the falling distance from the end of the delivery tube to the sand already in the chamber, and the mass of the particular sand delivered were controlled. Features intended as analogues to channel cut-and-fill facies were created by keeping the positioner stationary while sand was being added to the chamber. Continuous layers were created by programming the positioner to travel back and forth across the chamber while delivering sand at a uniform rate.

The heterogeneity structure, shown in Figure 1, was designed to represent a qualitatively realistic sequence of three lithologic units of different texture. Three commercially available, translucent, hydrophilic silica sands with narrow, non-overlapping grain size distributions were chosen to compose the three units (Accusand 12–20, a coarse sand; 30–40, a medium sand; and 50–70, a fine sand) (see Table 1). We created unit shapes reminiscent of those seen in channel cut-and-fill deposits but with vertical exaggeration. Fine sand emplaced along the edges of the chamber removed possible preferential flow of the nonwetting phase along the chamber boundaries.

We also packed an additional chamber where we maintained the continuity of the thin layer of fine sand stretching across the chamber about two thirds of the way toward the outlet from the injection port (see Figure 1). We refer to this pack as the secondary heterostructure, while the other we refer to as the primary heterostructure. We used this small, yet critical, difference between the primary and secondary heterostructures to demonstrate the sensitivity of TCE migration behavior to the lateral continuity in capillary barriers.

In each of the experiments the chamber was oriented so that the invading nonwetting phase was introduced in a density-unstable manner. That is, TCE (more dense than water) was introduced from the top, while CO₂ (less dense than water) was introduced from the bottom. For the sake of comparison, both nonwetting fluids advanced in the same direction through the heterogeneous structure. That is, TCE advanced downward through the structure just as shown in Figure 1, while CO₂ advanced upward, with the structure oriented upside-down to that shown in Figure 1.

After filling and orienting the chamber, we settled the sand with capillary forces and localized vibration. Beginning with an air-dried sand-filled chamber, we displaced air with CO₂ through the bottom manifold. Gas flooding was followed by

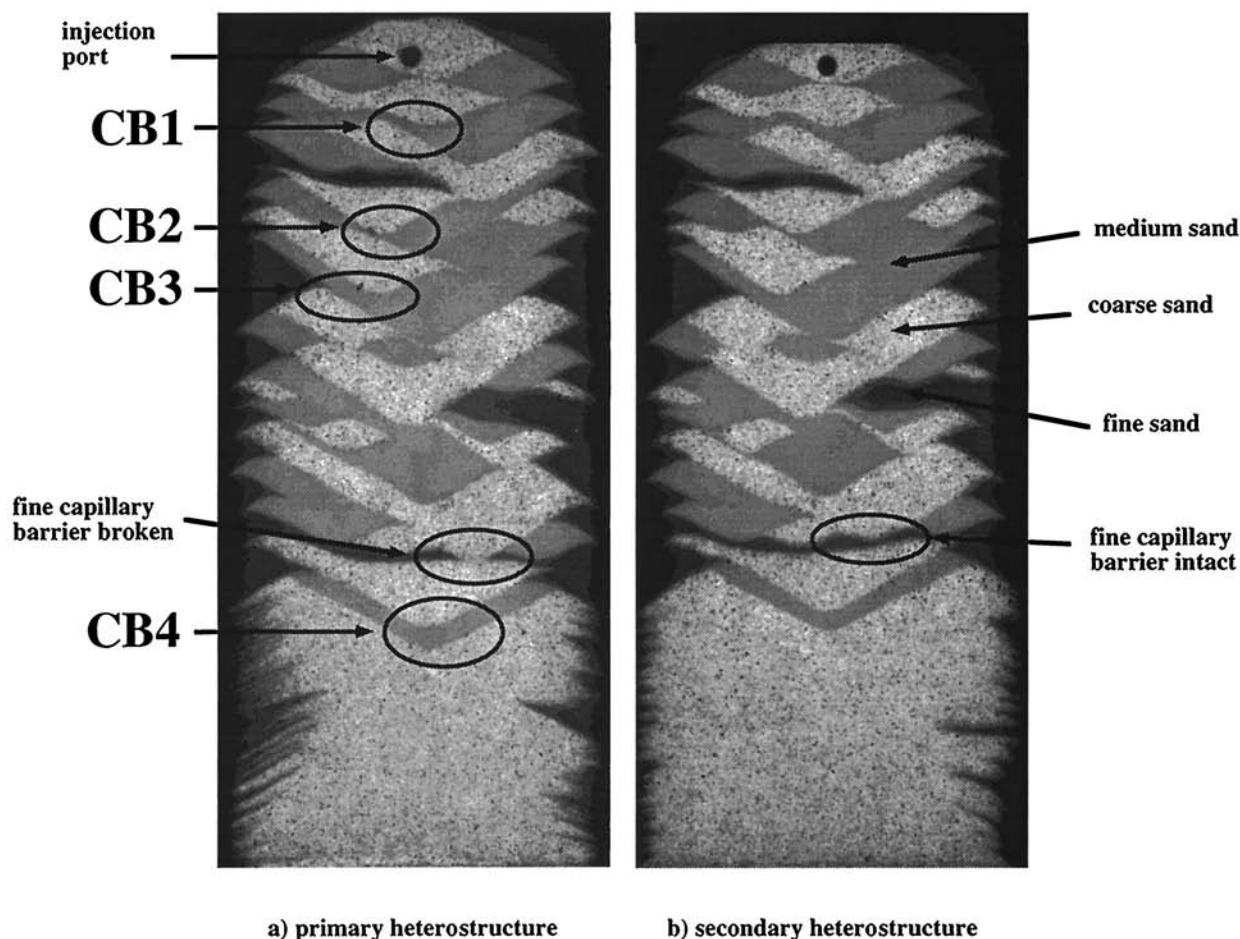


Figure 1. Digital images of the heterogeneous sand packs used in the invasion experiments. In these images the coarse sand transmits the most light and hence is the lightest; the medium sand appears gray; and the fine sand appears dark. The injection port and four major capillary barriers (labeled CB1 through CB4) are identified for the primary heterogeneous structure. These capillary barriers occur where medium sand separates coarse facies from one another. These same features can be found on the secondary heterogeneous structure as well. The difference between the (a) primary and (b) secondary structures can be seen in the fine-sand layer extending across the column about two thirds of the way from the top. In the primary structure this layer is discontinuous, while in the secondary structure this layer is continuous and forms one additional capillary barrier. The primary structure was used for experiments 1 and 2, and the secondary structure was used for experiment 3. Notice that small variations in facies location and shape exist between the two sand packings. These small differences had negligible effect on the behavior of the migrating fluids.

gravity-stabilized and viscous-stabilized flooding with degassed, deionized water until the chamber was saturated. We then drained the chamber through the bottom porous plate under suction, air entering from above. We continued pulling filtered dry air through the chamber and porous plate using a vacuum pump until the sand in the chamber was dry. The front of the chamber was then tapped with a hard plastic cylinder (a

screwdriver handle) to enhance further settling with localized vibration. This CO₂-water-drainage-drying-tapping cycle was repeated several times causing the heterogeneous packed sand structure to settle. Digital images of transmitted light through the chamber showed that the vast majority of the settling was achieved after two cycles.

Close comparison of the settled primary and secondary heterostructures shows small variations in shape and lens interface orientation between the two packs. Additionally, because the chamber was disassembled between experiments for cleaning, reassembly slightly changed the distance between the two glass plates thus causing the entire heterostructure to “scale” slightly in the vertical direction.

Table 1. Sand Properties

Sand	Sieve Size	Grain Size Mean, Maximum, Minimum mm	Porosity	Intrinsic Permeability, cm ²
Coarse	12–20	1.1, 1.7, 0.84	34.8	6.32E-06 ^a
Medium	30–40	0.05, 0.60, 0.42	35.4	1.20E-06
Fine	50–70	0.26, 0.30, 0.21	36.2	2.97E-07

^aRead 6.32E-06 as 6.32×10^{-6} , for example.

2.3. Material Properties

Pressure-saturation curves for each of the three sands were measured within the chamber for the air-water fluid system using the light transmission method. The chamber was filled

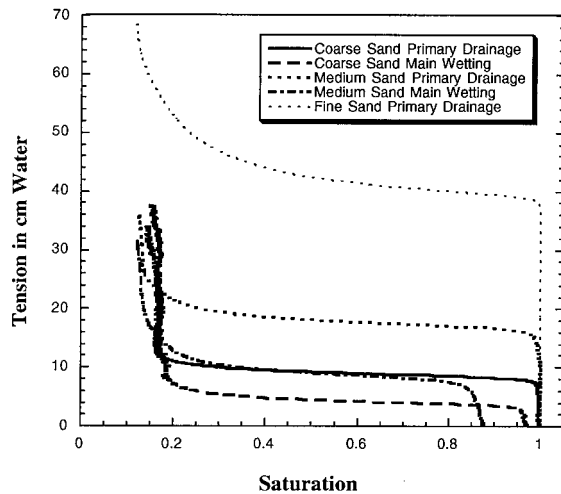


Figure 2. Hysteretic pressure-saturation curves (air-water) for the three sands used within the heterogeneous sand packs. The experimental chamber was packed uniformly with each of the three sands, and the light transmission method was used to measure equilibrium saturation profiles to yield the primary drainage curve (fully water-saturated initial condition) and the main wetting curve (residual nonwetting air-phase initial condition). The main wetting curve for the fine sand was not measured.

with a single sand type following the homogeneous filling method of *Glass et al.* [1989b]. A sequence of filling and drainage experiments to equilibrium points yielded primary wetting and drainage curves for the media [e.g., *Norton*, 1995] (see Figure 2). Porosity and saturated permeability were also measured during this characterization sequence and are presented in Table 1.

Fluid properties are given in Table 2. Interfacial tension (IFT) measurements were made using a Fisher Model 20 surface tensiometer following the manufacturer modified ASTM D 971-91 method [*American Society for Testing and Materials*, 1991]. Fluids were equilibrated for 2 min before IFT was measured. Fluid viscosity for the TCE was measured using a Cannon-Fenske viscometer following procedures recommended by the manufacturer. TCE density was measured with a pycnometer. Because we added Oil-Red-O dye (0.9 g/L) (Fisher Scientific, Pittsburgh, Pennsylvania) to the TCE in our experiments, we measured the properties of the dyed liquid. The presence of dye was found to decrease interfacial tension of the TCE.

2.4. Invasion Experiments

We conducted three invasion experiments (see Table 3). In our first experiment we injected CO_2 from the bottom into the

Table 2. Fluid Properties

Fluid	Density, g/mL	Interfacial Tension, dyn/cm	Viscosity Poise
CO_2	0.002 ^a	71	1.48E-02 ^a
H_2O	0.996 ^a	NA ^b	1.00E-02 ^a
TCE	1.464	27	5.75E-03

^aValues are from *Weast* [1985].

^bNA is not applicable.

Table 3. Experiments Conducted

Fluid/Fluid System	Heterogeneous Structure	Q , mL/min	System Breakthrough, Redistribution	
			mL	End, min
$\text{CO}_2/\text{H}_2\text{O}$	primary	1.2	50.8	NA ^a
TCE/ H_2O	primary	0.9	73.1	303
TCE/ H_2O	secondary	1.0	158	240

^aNA is not applicable.

water-saturated primary heterostructure. After conclusion of the experiment the CO_2 was dissolved away with deaired water, and the chamber was inverted. We then performed our second experiment by injecting TCE from the top. After emptying, cleaning, and repacking the chamber with the secondary heterostructure, we then conducted our final experiment with TCE injected from the top. Each invasion experiment started from the fully water-saturated state verified with the light transmission method. Outflow occurred from the side opposite injection and was connected to a tube directing the water to a reservoir on a scale with a drip point 1.5 cm above the top of the chamber. Prior to starting the CO_2 invasion experiment, we displaced the degassed, deionized water in the chamber with CO_2 -saturated water. This minimized the dissolution of the free-phase CO_2 into the pore water as CO_2 invasion progressed.

An 18-gage needle (0.84 mm ID) was used to inject the nonwetting fluid into the coarse sand. For the TCE experiments, liquid was injected using a syringe pump, while for the CO_2 experiment, gas was delivered to the chamber from a pressure bottle through a metering valve and flow meter. Injection rates were designed to be ~ 1 mL/min for all experiments (see Table 3) so that average viscous forces would be small. The mass of water leaving the chamber was measured every 30 s with a computer-monitored electronic balance to yield the displaced volume as a function of time. For the TCE-water experiments, Oil-Red-O dye (0.9 g/L) was added to the TCE to enhance visibility. For the CO_2 -water experiments, changes in fluid saturation were easily measurable without dyes because of the very different refractive indices between gas and water. Fluid injection was terminated when the leading edge of the nonwetting phase had reached the far side of the chamber. Redistribution of the nonwetting phase was monitored for the TCE experiments over a several day period.

2.5. Image Collection and Processing

The experimental chamber was placed between a controlled output diffuse light source and a digital camera that measures the intensity of light transmitted through the chamber as a function of space and time. Digital images were acquired at a rate of one image every 20 s (or ~ 1 image per 0.33 mL of injected fluid) with a 12-bit shuttered digital camera (1317 \times 1035 pixels and 4096 gray levels) using a 60-mm lens and ~ 0.1 -s exposure time to record intensity fields from a distance of 4.3 m within a dark room. Camera resolution was ~ 0.5 mm per pixel (0.25 mm²/pixel).

We processed digital images to yield saturation fields as a function of space and time and then used these images to create "composite" fields that summarize (1) the movement of the nonwetting invasion front in time and (2) cyclic temporal variations in saturation behind the front. Preliminary to this, images were first preprocessed to adjust the intensity field for

small fluctuations of the light source using a photographic constant-density stepped wedge (included in every image) and to realign the image for occasional small shifts between the camera and the test cell (tolerance of 0.05 pixels).

Saturation fields were calculated using modifications of techniques presented by *Tidwell and Glass* [1994] for both refraction-dominated and absorption-dominated energy transmission within homogeneous media. For the CO₂-water experiments where light passage is dominated by refraction, we used their theoretical development to calculate pointwise the number of pores (their k) from the saturated and dry images and then used this “ k field” to calculate the transient saturation fields. For the TCE-water systems where the refractive index of the fluids is nearly the same, saturation was calculated using energy absorption by the Oil-Red-O dye analogous to their X-ray transmission. However, because a fully saturated Oil-Red-O dye image was not obtained, we substituted the low-intensity dry image and scaled it to yield saturation values within pools of the coarse sand near the expected value of 0.83 (see Figure 2). This approach, while approximate for sands other than the coarse, maintained excellent spatial definition of the saturation field. Other inaccuracies were also noted in the experiments. Inspection of the saturation fields showed highly variable saturation when the nonwetting phase did not fully span the thickness of the sand, that is, when the saturation is not uniform from the front wall to the back wall of the chamber. Additionally, where high nonwetting phase saturation regions were next to completely water-saturated regions, the scatter of light caused blurring of the sharp transition. To estimate the gross error associated with our saturation fields, we compared volumes of injected nonwetting phase as calculated from saturation fields against the known injected volumes. Total nonwetting volume error was a maximum of 12% across the three experiments. While these gross errors can be reduced through additional calibration, error within the field where the nonwetting phase does not fully span the thickness of the pack and where high- and low-saturation regions are juxtaposed will remain. However, for the tracking of the invasion front and subsequent analysis of saturation dynamics, saturation errors are of secondary importance.

To track the progression of the advance of the nonwetting phase, we used the individual saturation images taken over time to create a composite order image that shows the advance of the invasion front. This order of invasion image is built by tracking the first nonwetting saturation increase above system noise at each point within the field. In building a composite order image, some pore-scale detail is lost as we ignore the degree of saturation. However, using this method, we are able to define the extent of the invading phase with excellent precision as a function of time throughout an entire experiment in a single image.

To analyze the local monotonicity of saturation in time within the field, we compared sequential saturation images and counted the number of cycles from increasing to decreasing saturation above system noise at each pixel in time. A cycle image shows locations where saturations increase and decrease. Values in the cycle images of 1 and above indicated that a location behaved nonmonotonically as the experiment progressed. We note that while cycle images give an indication of internal dynamics behind the initial invasion front, they weight early invasion regions higher than later invasion regions. Additionally, they will not catch all cycles if the period of the

pulsation is less than our 20-s acquisition interval between images.

3. General Invasion Results

Use of the light transmission technique allows us to observe, record, and analyze the invasion process with unprecedented clarity. In this section we present general invasion results through a series of images that show (1) nonwetting phase structure at the conclusion of fluid injection, (2) development of this structure in time, (3) phase saturation nonmonotonicity as this structure evolves, and (4) subsequent redistribution of the nonwetting phase. Note that all images are oriented such that flow is in the same direction to facilitate comparison. That is, the CO₂ invasion is rotated 180° with gravity now acting upward in the image.

Plate 1 shows saturation structures when the CO₂ or TCE had just spanned the system and injection was terminated. We see that the nonwetting fluid is confined mainly to the coarse units and is composed of a number of “pools” behind capillary barriers (CBs) and “fingers” that penetrate CBs and connect the pools together along a pathway. The continuity of the fine unit in the secondary heterostructure (Plate 1c) creates a significant TCE pool ~2 times deeper than found in the primary heterostructure. Saturation within the coarse unit pools is near uniform and at the nonwetting saturated value is consistent with our calibration. The local scatter of light blurs the saturation field around sharp transitions at the edges of pools and thus shows artificial nonzero nonwetting saturations in the surrounding capillary barriers. Overestimation of the saturation is particularly noticeable in the fine CB (broken in the primary heterostructure) as it is both thin and has nonwetting fluid on its top and bottom. Also, note in the secondary heterostructure that maximum saturations within the medium sand in the pool above the fine CB are underestimated because of our lack of a fully TCE-saturated image for saturation calculations.

The saturation within fingers is much more variable than within pools. This is further shown in magnified and contrast-enhanced images of the final saturation structures at and beyond CB4 for CO₂ and TCE in the primary heterostructure (Figure 3). The highly variable appearance of the saturation along a finger demonstrates that the fingers are not smooth macroscopic features. We see that the appearance of fingers in the coarse unit as a series of near disconnected regions of high saturation is due to the “pore-scale” nature of the fingers amplified by the imaging technique. The finger is composed of a string of nonwetting clusters connected by single pores and thus does not uniformly fill the pore network between the front and the back of the chamber. This structure corresponds closely to the link/node/blob picture of a percolating backbone [e.g., *Stanley, 1977*] except that it is directionally oriented by gravity. When the finger is in pores near or at the front of the chamber, we see it as a discrete, connected pore structure. As the finger meanders farther behind the chamber front, it becomes increasingly blurred by the scatter of light. As seen in Plate 1 and Figure 3, the CO₂ invasion shows a more “slender” pathway with pools of lower height and narrower connecting fingers than that for the TCE invasions. Additionally, detailed evaluation at high magnification shows that all CBs were breached by a single finger for the CO₂ invasion, while multiple fingers extend through each CB for both TCE invasions.

Composite order images showing the invasion sequence for each experiment are presented in Plate 2. As discussed earlier,

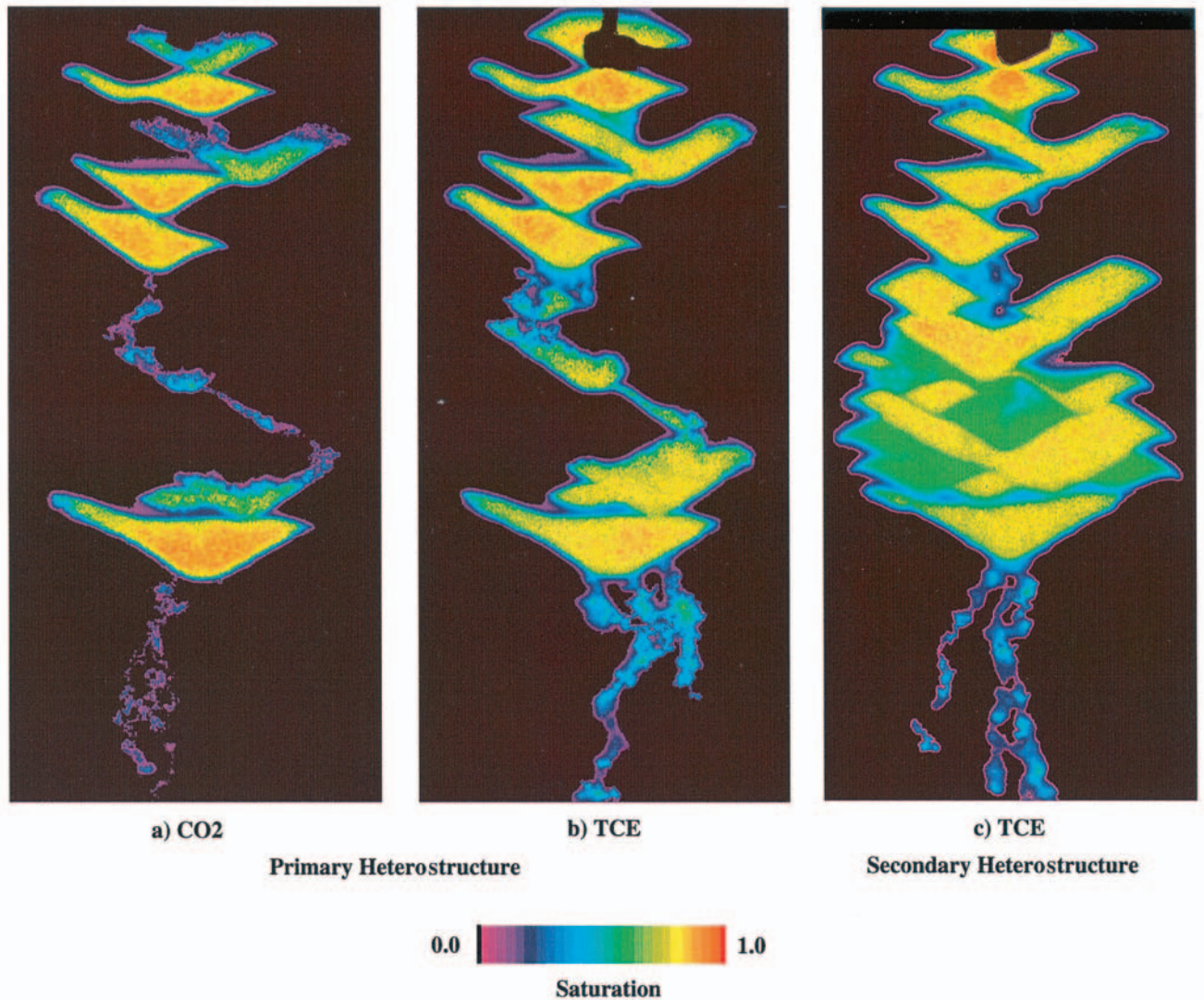


Plate 1. Nonwetting saturation fields at the time the invading nonwetting phase spanned the length of the chamber just before fluid injection was terminated: (a) CO₂ in the primary heterostructure, (b) tetrachloroethylene (TCE) in the primary heterostructure, and (c) TCE in the secondary heterostructure. Color indicates the local nonwetting phase saturation. Note that the local scatter of light blurs the saturation field around sharp transitions at the edges of pools and within finger zones. Also note that maximum saturations within the medium sand in Plate 1c are underestimated.

the fundamental pore-scale behavior is less obvious in these images as we simply track increases in nonwetting saturation above zero. The order images clearly demonstrate the heterogeneity structure to impose an oscillation between modes of gravity-destabilized and gravity-stabilized invasion. Near vertical fingers grow away from the source during the gravity-destabilized invasion mode, while flat horizontal fronts grow back toward the source during the gravity-stabilized mode. This dynamic is clearer at higher resolution as shown in Plate 3 composed of magnified and recolored zones of the order images containing CB1 and CB2.

In general, the gravity-destabilized finger growth mode occurs in all units until a CB is encountered. Once encountered, CBs then cause gravity-stabilized pool growth behind the CB until they are breached. During this mode the earlier gravity-driven fingering is partially or in some cases completely “overwritten” by the backward growing horizontal front. As the stabilized growth period progresses, if units of intermediate

texture are encountered (i.e., lower entry pressures than the primary CB), they are entered if the appropriate pressure is exceeded. This behavior is particularly well demonstrated in the secondary heterostructure TCE invasion where the continuity of the fine-textured CB was maintained. Refer to the green and yellow regions in the composite order image (Plate 2c) while also looking back to the heterostructure image (Figure 1b). Notice that medium units and coarse-textured units were being filled concurrently, the medium units at lower elevations than the coarse units.

As nonwetting phase pressure builds behind a CB, entry of the barrier begins at a series of points along the interface from which small fingers grow. When one or more of these fingers reach the far side of the barrier, the barrier is breached, and the fingers continue growing into the underlying layer. For the CO₂ invasion, only the leading finger that is first to enter the coarser layer ever continues growth. However, for both TCE invasions several of the lagging fingers always make contact

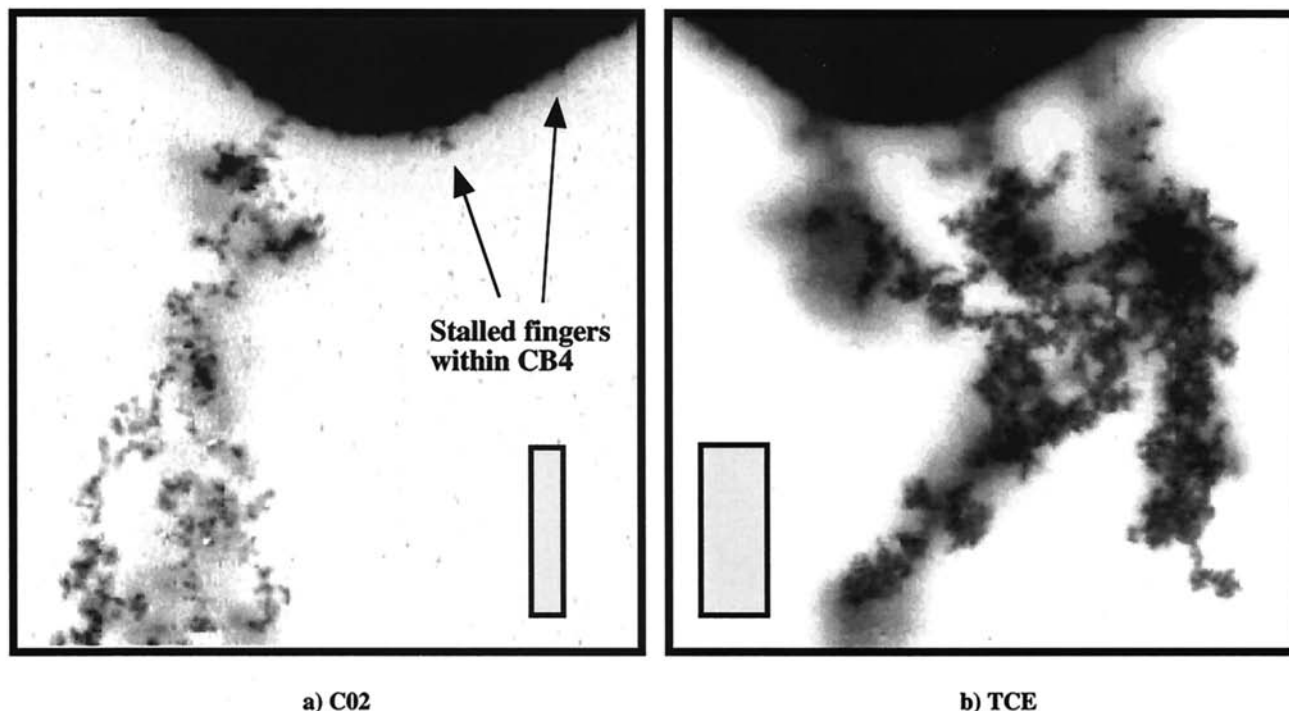


Figure 3. Magnification of nonwetting saturation structure at and beneath CB4 in the primary heterostructure: (a) CO₂, and (b) TCE. Saturation fields have been contrast enhanced to bring out the underlying pore-scale nature of the fingers as a string of clusters connected by single pores. Note that the two stalled fingers within CB4 marked for CO₂ continued growing for TCE and spanned the capillary barrier. Boxes shown are representative finger widths of 0.6–0.7 and 1.2–1.3 cm for CO₂ and TCE, respectively.

with the underlying coarser layer and generate separate fingers beyond. For TCE invasion the pool height behind the capillary barrier continues to rise during this period and stops after the final finger spans the capillary barrier. However, for CO₂, pool height stops increasing as soon as the first finger spans the barrier. Close study of Figure 3 shows that the initial growth points in the primary heterostructure are identical for both the CO₂ and TCE experiments; however, for TCE all three fingers continued to grow.

Animation of sequential saturation images for all experiments clearly shows that the nonwetting phase saturation does not increase monotonically in time at all locations along the invasion pathway. The spatial structure of this nonmonotonicity up to the conclusion of injection is shown in Plates 4a and 4b for the TCE and CO₂ invasions in the primary heterostructure. Color represents the number of increase-decrease cycles that occurred as invasion proceeded. For the CO₂ experiment we see pulsation through nearly the entire gas invasion structure. Maximum cycles reached 18 within a small region beyond the breach of CB1. For TCE invasion in the same pack we find pulsation concentrated directly beyond CB3 where it reached values of 15. A second region within the fingering zone below CB4 has undergone a single cycle by the time of system breakthrough. Pulsation in the secondary heterostructure TCE invasion (not shown) was similar but more subdued reaching a maximum value beyond CB3 of 4. Again, we note that cycle counts could have been higher than we measured as our acquisition interval was only 20 s.

Close examination of animations and magnifications of the cycle images (see Plate 5) show pulsation to occur at two different scales: pore scale and pool scale. In pore scale pul-

sation, individual pores and clusters of pores are seen to “drip” in time. Such pulsation can be seen within one CB (e.g., CB1 in CO₂ injection) and within the coarse unit directly below CBs and along fingers. In pool scale pulsation, entire pools “throb” in time. High cycle values are found both in the large region at the top of the pool and along the edges of the pool where pores repeatedly fill with wetting and nonwetting phases in concert. This larger-scale throbbing is seen within the pools behind all CBs in the CO₂ invasion but is not detected within the TCE invasion structure. A glimpse at the temporal complexity of pulsation within our experiments is shown in Figure 4 where nonwetting fluid saturation is plotted as a function of time for a series of small ~25-pixel regions located along the CO₂ invasion structure. We see that while the traces may look generally periodic, they are not. At each location both the magnitude of the saturation swing and the local period are different from one pulse to the next, the small “hot spots” within and below capillary barriers showing a more erratic pulsation than the pools.

When the invading fluid reached the distal end of the chamber, nonwetting injection was terminated, and the redistribution phase of the experiment began. For the CO₂ invasion, negligible redistribution occurred. However, for the TCE, redistribution lasted several hours (see Table 3). A fine layer at the bottom of the chamber kept the TCE within the chamber, so simultaneous drainage and invasion could be visualized. Figure 5 shows the difference between the beginning and end of the redistribution stage for the TCE invasions into the primary and secondary heterostructures; dark zones indicate where TCE has drained, bright zones indicate where it has moved, and shaded zones indicate where no change occurs.

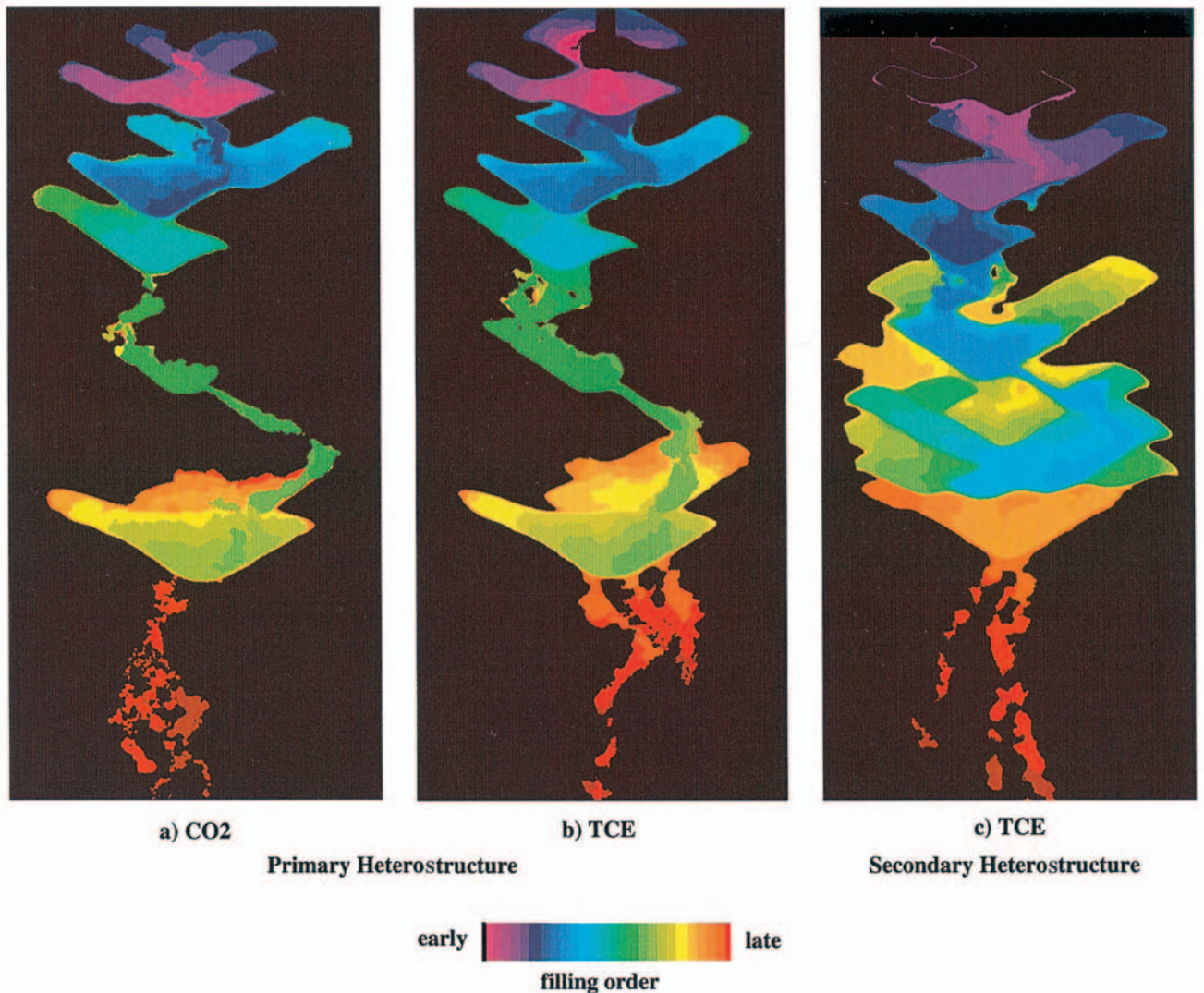


Plate 2. Composite order images of nonwetting invasion: (a) CO₂ in the primary heterostructure; (b) TCE in the primary heterostructure; and (c) TCE in the secondary heterostructure. Color indicates the order of filling. In Plate 2c initial data were lost resulting in the black region at early times at the top of the chamber.

More fluid redistributed for the secondary heterostructure than the primary structure as can be seen by the depth of pooled TCE at the bottom of the cell. Visual inspection of the drained zones of pools and fingers within the coarse unit show the TCE to be entirely trapped in a series of blobs/ganglia at a residual saturation of ~ 0.2 – 0.3 . Still, a majority of the mass is held in the pools at high saturations of ~ 0.8 – 0.9 . During redistribution we also find significant pulsation to occur, much greater than during the initial invasion. Plate 4c shows a cycle image built over the redistribution period for the primary heteroexperiment. Pulsation is found as TCE moves through the coarse run between CB3 and CB4 and beyond CB4 as we saw in the CO₂ experiment. An additional finger below CB4 also formed and pulsated below CB4, the main pulsation point just overlapping that for the CO₂ experiment beyond this barrier.

In summary, we see the following:

(1) CBs create a pool and finger invasion structure. Pore-scale fingers occur as interconnected clusters of nonwetting phase resulting in highly variable macroscale saturation. Pools

occur as macroscale zones of high saturation. The vast majority of the nonwetting phase mass is held in the pools.

(2) Gravity-driven fingers always occur as invasion proceeds away from the source. Gravity-stabilized invasion can overwrite the fingers when a CB is encountered and a pool-forming horizontal front grows backward toward the source.

(3) Pulsation occurs within fingers and within pools at different scales of expression for each. Pulsation was most pervasive for CO₂, and in the TCE experiments; pulsation increased as redistribution commenced.

(4) Redistribution after termination of injection occurred for TCE but not for CO₂. As we will show in section 4, this difference results from the importance of viscous forces at the flow rates imposed to increase TCE pool heights during invasion over their equilibrium or final static levels.

In section 4 we focus on defining a suite of length scales that describe the evolving and dynamic invasion structure generated by the nonwetting phase within a heterogeneous porous medium.

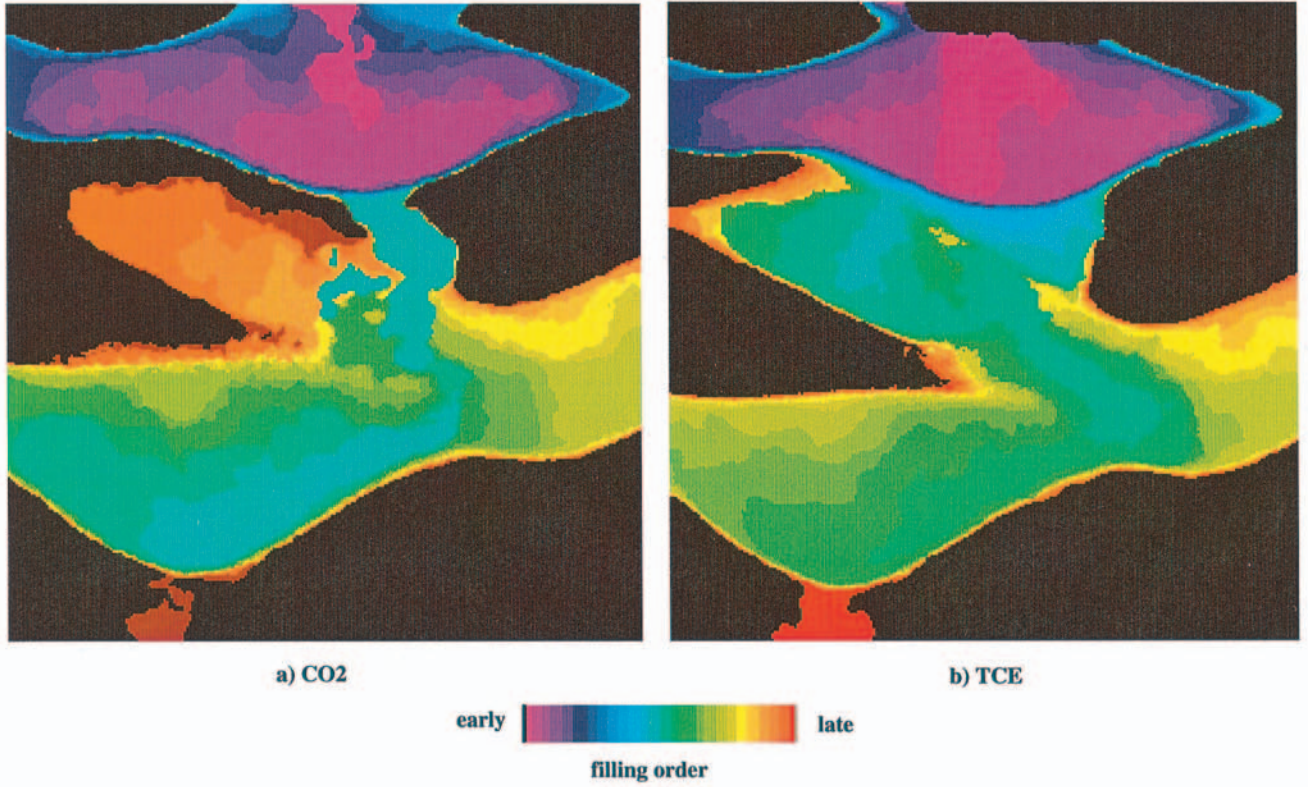


Plate 3. Magnification of the composite order images of nonwetting invasion in the vicinity of CB1 and CB2 in the primary heterostructure: (a) CO₂ and (b) TCE. Color indicates the order of filling.

4. Length Scales for Invasion Structure and Dynamics

Invasion structure and dynamics within the granular pack can be analyzed by considering local differential pressures within the invading phase ΔP_i , associated with capillary, gravitational, and viscous forces (subscripts c , g , and v , respectively) written as

$$\Delta P_c \sim 2\sigma \left(\frac{1}{R_{\min}} - \frac{1}{R_{\max}} \right) \quad (1)$$

$$\Delta P_g \sim \Delta \rho g h_g \quad \Delta P_v \sim Q \mu h_v / kA,$$

where σ is the interfacial tension, $\Delta \rho$ is the density differential (positive) between fluids, g is the gravitational constant, h_g is a local macroscopic vertical distance, Q is the flow rate, μ is the viscosity of the invading fluid, h_v is a local macroscopic length in the direction of invasion, k is the permeability, and A is the local cross-sectional area of the invading fluid-filled porous media. Note that k applies to the structure being considered, that is, a string of pores within a finger or a “matrix” of pores within a pool and will be approximated by the intrinsic permeability of the media within A . R_{\min} and R_{\max} represent radii of curvature for the pore-scale fluid-fluid interface typical of the minimum and maximum, respectively, encountered locally such as to consider variability in capillary forces within a unit, between units, or between wetting and nonwetting entry, depending on the situation of interest. As written, ΔP_i are all positive quantities.

Considering fluid properties alone (see Table 2), we see that CO₂ has slightly larger ΔP_c and ΔP_g than TCE (within a factor of 2–3), while TCE has significantly larger ΔP_v (factor of 39).

Ratios of the ΔP_i yield dimensionless numbers such as the bond number (gravity/capillary) or the capillary number (viscous/capillary) which can be used to define the regime in which our experiments lie. For a heterogeneous system such as ours, these numbers will vary as a function of time and space and thus are less defining than in homogeneous media.

Here we use simple local-scale analyses that balance the local pressure differentials, that is,

$$\Delta P_c + \Delta P_g + \Delta P_v = 0, \quad (2)$$

to derive approximate relations for a set of local macroscopic length scales that control phase invasion structure and dynamics within the heterogeneous system. The sign of each ΔP_i in (2) depends on its action with respect to the situation of interest. We consider length scales for finger diameter, finger pulsation, maximum pool height, pool pulsation, and minimum pool height and evaluate derived formulations with respect to experimental observations. In all cases we find that the intrinsic pore-scale nature of the invasion process and resulting structure must be incorporated into our analysis to explain experimental results. In this our analysis departs from standard scale analysis for continuum scale flow in porous media where assumed governing equations (usually partial differential equations for conservation of mass, momentum, and energy) are used to develop such relations [e.g., *Began*, 1985]. Given the pore-scale control within our problem, such macroscopic continuum approaches applied at a typical REV scale to the porous medium are not fully applicable.

4.1. Finger Diameter

As described in section 3, fingers are composed of a series of clusters connected or “strung” together by single pores yielding

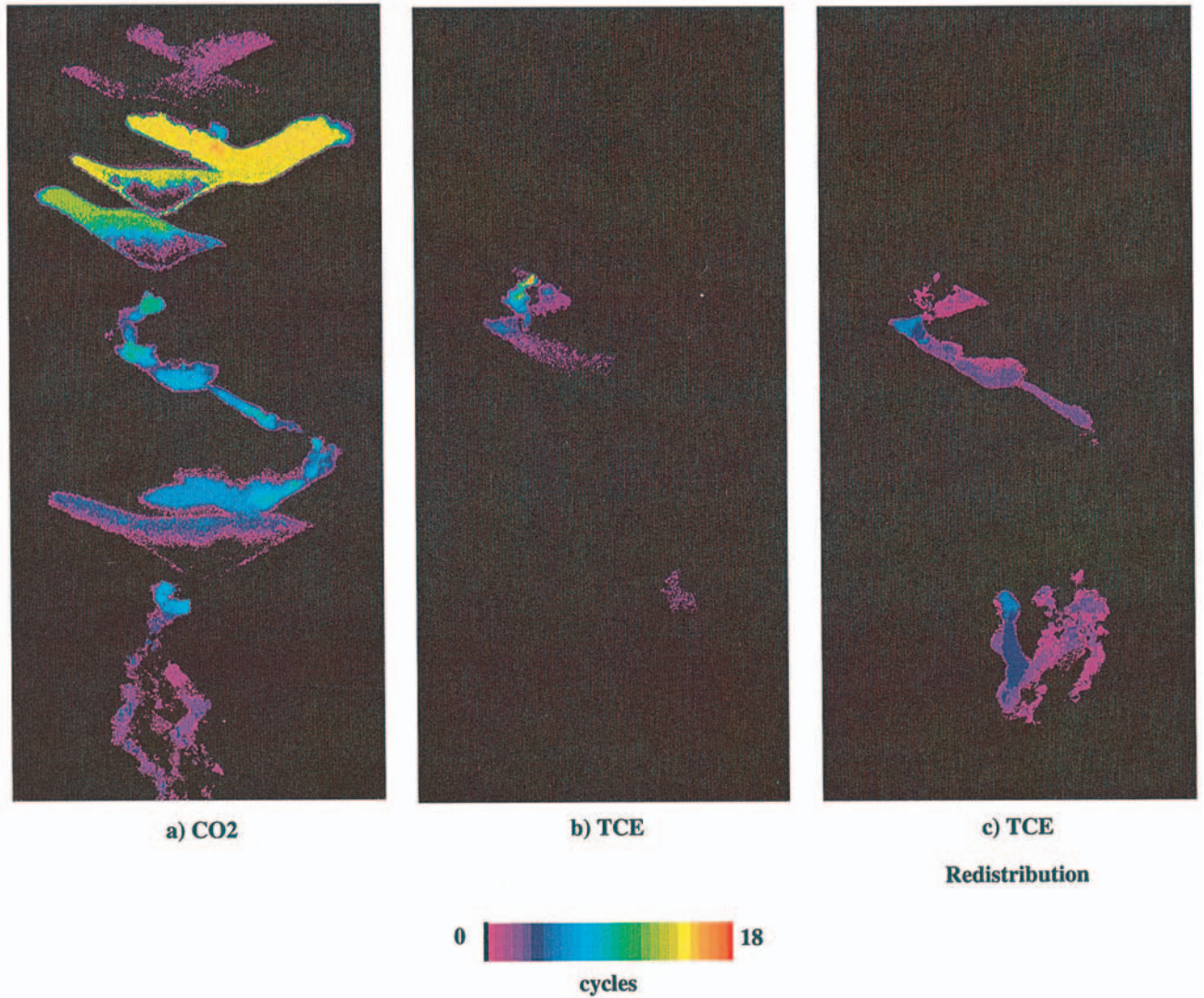


Plate 4. Fluctuation cycle images for saturation of the nonwetting phase in the primary heterostructure: (a) CO₂ during invasion; (b) TCE during invasion; and (c) TCE during redistribution. Color indicates the number of cycles of saturation increase then decrease.

a highly variable finger diameter (see Figure 3 and Plate 3). These clusters form because of the random nature of the capillary pressure required to fill individual pores within the network. Additionally, we observe that a finger grows through a series of “bursts” where a small capillary finger moves forward rapidly across a single pore at or near the fingertip and then stops, followed by local “backfilling” to create a wider cluster. Therefore we conclude that capillary pressure oscillates between a low value somewhere within the backfilling cluster (R_{\max}) and a high value just before the next burst occurs as the single “critical” pore is entered (R_{\min}). Observationally, we can also conclude that owing to the “stringed cluster” nature of the finger, viscous forces acting against flow along the finger are controlled primarily within a single to several pore cross-sectional area composing the primary conductive backbone of the nonwetting finger. Along the backbone we consider k to be approximately the intrinsic permeability of the granular media.

To yield an approximate macroscopic length scale for finger diameter, we consider a local balance of ΔP_c that creates the clusters we associate with the diameter to $\Delta P_g - \Delta P_v$ that

drives directional finger growth. At the scale of the finger diameter d we take $h_g = h_v = d$ and find

$$d \sim \frac{2\sigma}{\Delta\rho g - \frac{Q\mu}{k_f A_f}} \left[\frac{1}{R_{nw \min}} - \frac{1}{R_{nw \max}} \right], \quad (3)$$

where $R_{nw \min}$ and $R_{nw \max}$ are the average minimum and maximum radii, respectively, sampled during finger growth and subscript f refers to the finger. Here we consider A_f to be independent of d as d is controlled by the average cluster size along its length, while A_f is restricted to the conductive backbone within the finger. $R_{nw \min}$ is a function of the pore size distribution and its connectivity within the sand thus yielding a dependence of d on pore size distribution such as found in the analysis of *Glass and Yarrington* [1996]. Additionally, $R_{nw \min}$ will be dependent on gravity and viscous forces active in the media, gravity forces increasing and viscous forces decreasing $R_{nw \min}$ sampled. We note that (3) has a similar form to that of *Glass et al.* [1989a, 1989b], derived through a combination of

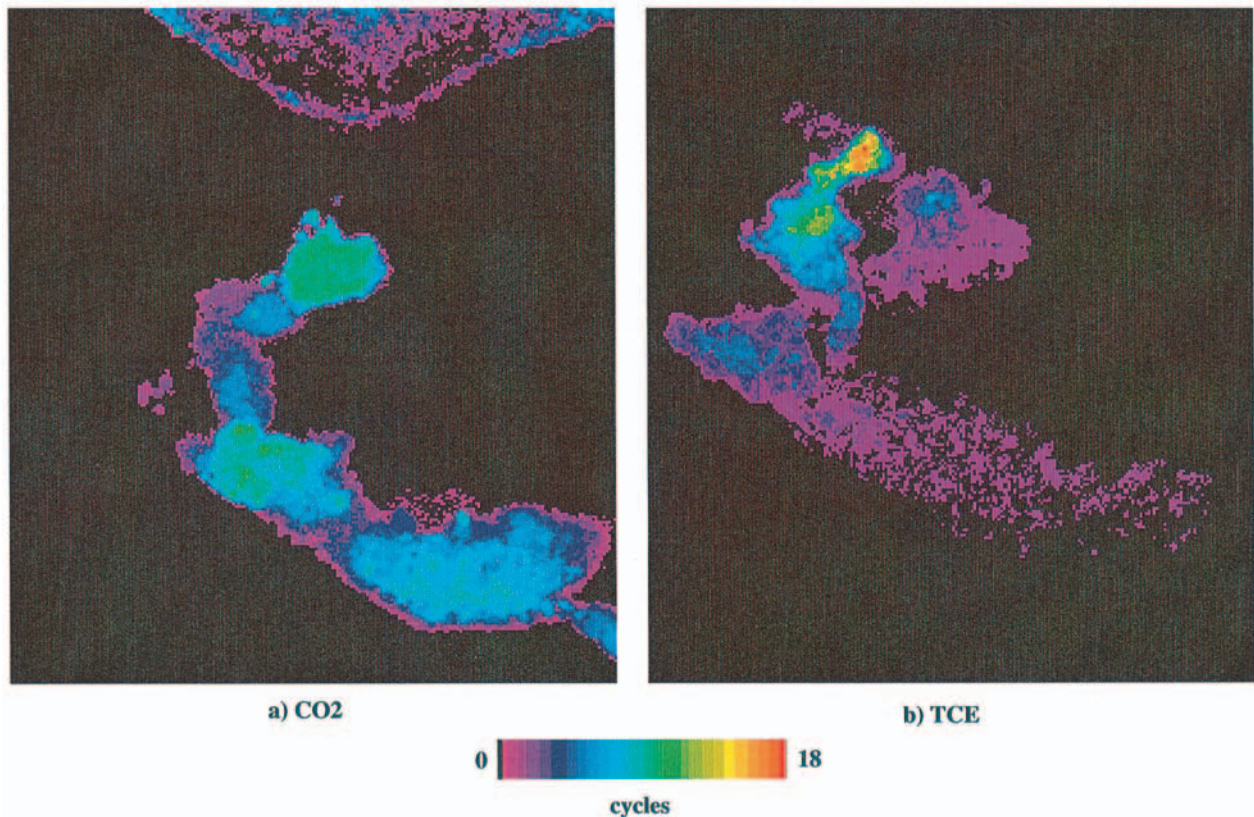


Plate 5. Magnification of fluctuation cycle images in the vicinity of CB3 for the primary heterostructure: (a) CO₂ and (b) TCE. Color indicates the number of cycles of saturation increase then decrease.

dimensional analysis and experimentation for gravity-driven wetting fingers. There, however, the macroscopic sorptivity evaluated between wetting entry and the saturation (or pressure) within the finger was used to represent the influence of

finger-widening capillary forces. Additionally, for wetting invasion, fingers are macroscopic, and so A_f is tied to the finger diameter. Note that for nonwetting invasion considered here, capillary forces oppose finger widening, and thus finger diameter above that of a single pore is due to the invasion process within a network of variable pores.

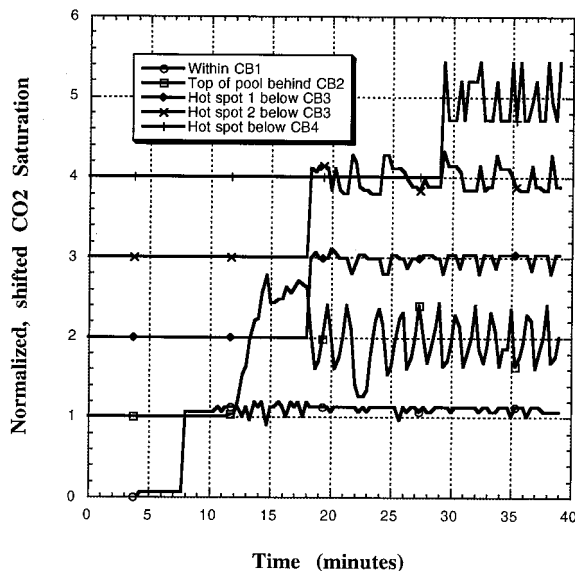


Figure 4. Time series of saturation at various locations during nonwetting phase invasion for the CO₂ experiment illustrating chaotic fluctuations in saturation. Saturation data have been normalized by the mean at each location and shifted so that saturation histories may be compared.

Because of the pore-scale nature of fingers, experimental diameters are difficult to measure. However, we estimate them below CB4 for the CO₂ and TCE experiments to be ~ 0.6 – 0.7 and ~ 1.2 – 1.3 cm, respectively (see Figure 3). Additionally, below CB4 we note that three fingers formed for both TCE experiments. In order to compare (3) to these estimates, we must obtain values for the various parameters within the relation. We take $R_{nw \max}$ as the air entry value of the drainage pressure-saturation curve for the coarse sand of ~ 0.0192 cm, assuming contact angles for all systems are the same. $R_{nw \min}$ can also be estimated from the drainage pressure-saturation curve at a representative fluid saturation for the finger. Neglecting the gravitational or viscous dependency of $R_{nw \min}$, we first consider an average effective fluid saturation derived from standard percolation theory. Considering a random, spatially uncorrelated network of pores within a cubic lattice, the percolation threshold is found to be ~ 0.3 [Stauffer and Aharony, 1992, p. 17]. Estimating the effective nonwetting saturation S_{enw} by this value (assuming all pores to have the same volume) yields $R_{nw \min}$ of ~ 0.0173 cm for the coarse sand from the drainage pressure-saturation curve. Neglecting viscous forces in (3) yields finger diameters of ~ 0.8 and 0.7 for CO₂ and TCE, respectively. If we now consider the experimentally measured saturations within the fingers for CO₂ of ~ 0.15 – 0.20

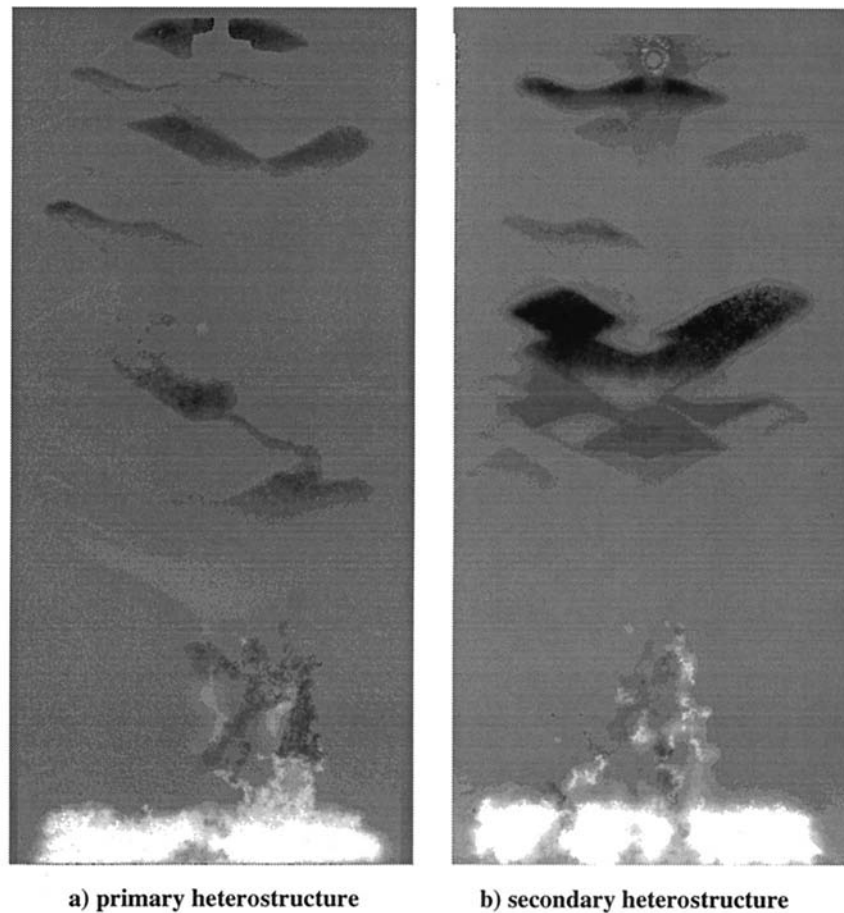


Figure 5. Redistribution of nonwetting phase at the conclusion of invasion for the TCE experiments: (a) TCE redistribution in the primary heterostructure and (b) TCE redistribution in the secondary heterostructure. Dark zones indicate locations where TCE has drained. Light zones indicate locations to which the TCE has migrated.

and for TCE of ~ 0.35 – 0.40 , $R_{nw \text{ min}}$ ranges are ~ 0.0178 – 0.0176 and ~ 0.0169 – 0.0166 cm, with corresponding finger diameters of ~ 0.6 – 0.7 and ~ 0.8 – 1.0 , respectively. For CO_2 our prediction now overlaps. Assuming that each TCE finger carries a third of the flow, including viscous forces with experimental parameters for k and Q , if we take A_f equivalent to \sim three pores ($\sim 3 \delta^2$, where δ is the mean grain size for the unit), d increases to ~ 1.2 – 1.3 cm for TCE (no change for CO_2 for a single finger carrying the full supplied flow). Thus finger width can be matched reasonably well with (3) if we consider the finger's pore-scale nature.

4.2. Pulsation Within a Finger

As a finger lengthens, we find the wetting fluid reinvades selected pores a distance behind the fingertip. This happens as hydrostatic gravity forces act against viscous and hysteretic capillary forces along the vertical length of the finger. Here the differential capillary pressure of interest is between the nonwetting invasion at the fingertip and the wetting invasion behind. If we consider a local balance of differential pressures from the fingertip backward, we find that as the finger grows vertically, gravity allows the reinvansion of pores with the wetting fluid when the finger reaches an average vertical tip length h_t :

$$h_t \sim \frac{2\sigma}{\Delta\rho g - \frac{Q\mu}{k_f A_f}} \left[\frac{1}{R_{nw}} - \frac{1}{R_w} \right], \quad (4)$$

where R_{nw} and R_w are average radii for nonwetting and wetting invasion within the unit, respectively. This process was first described by *Glass et al.* [1989c] for gravity-driven wetting fluid fingers. As we will see, for the nonwetting case considered here, the stringed cluster nature of the finger and the lack of connecting films once pores are reinvaded with the wetting phase imposes pulsation, while only a single oscillation is found for the wetting case.

The small critical pores connecting clusters along the finger form the critical links within the conducting backbone of the finger. On the basis of our earlier description of finger burst growth, these linking pores are also likely to be the smallest pores sampled and thus most likely to be reinvaded with the wetting phase. When they are reinvaded with the wetting fluid, the pathway is broken. Pressure within the upstream nonwetting phase must rebuild ~ 2 times wetting entry (see hysteretic curves in Figure 2) to reinvade a critical pore. After reinvansion with the nonwetting fluid, h_t , given by (4), is in time achieved again, the wetting fluid enters the critical pore, and the cycle begins again. Because gravity forces reduce the total pressure

back along the finger, other noncritical “ancillary” pores within the upstream cluster with slightly larger R also join the pulsation, first filling with the nonwetting phase until the critical pore is “opened” and then emptying until it is “closed.” Thus the upstream cluster grows and then shrinks, amplifying the pulsation induced and controlled by the downstream critical pore. As a finger grows beyond a length of h_t , it will contain a number of critical pores along its length where h_t is achieved, and thus the nonwetting phase fragments into a series of steady “residual” clusters connected by pulsating critical and ancillary pores. When a finger reaches a CB, the invasion mode switches from gravity-destabilized to gravity-stabilized invasion. As the pool grows back toward the source, pulsation is curtailed to a distance h_t from the edge of the growing pool back along the supplying finger.

While we found that finger diameter given by (3) is quite sensitive to the saturation within the finger and thus choice of the R values, (4) is not. If we estimate R_{nw} and R_w by an average value of S_{nw} and S_w of 0.3 from the pressure-saturation curves ($R_{nw} \sim 0.0172$ cm and $R_w \sim 2R_{nw}$), calculation of h_t with (4) for the coarse layer neglecting viscous forces yields values of ~ 4.2 and 3.4 cm for CO_2 and TCE, respectively. Experimentally, we find pulsation during the CO_2 experiment throughout the entire finger run between CB3 and the pool above CB4 as well as below CB4, thus supporting the inviscid value given by (4) for CO_2 . For TCE, however, only the two zones directly below CB3 and CB4 show pulsation, each >15 cm above the maximum pool height behind CB4 and the bottom of the chamber, respectively. Including viscous forces increases the TCE value calculated by (4) to ~ 15 cm for measured k and Q if we take A_f of $\sim 3.3 \delta^2$ with, again, no influence for CO_2 . Considering that three fingers form in the TCE experiment, this corresponds to $\sim 1.1 \delta^2$ per finger. We note that when viscous forces are important, (4) is very sensitive to the value of A_f and that to match the experimental results for TCE, it must be reduced from $\sim 3 \delta^2$ per finger found earlier for a growing fingertip with (3). This result further emphasizes the importance of the conducting backbone and reflects the decrease in its cross-sectional area from several pores at the fingertip down to a single pore controlling pulsation at h_t .

4.3. Maximum Pool Height

We can obtain a simple relation for maximum pool height behind a CB, $h_{p \max}$, by once again balancing local pressure differences for capillary, gravity, and viscous forces. The differential capillary force of interest is that required to enter pores within the coarse unit behind the barrier versus that to enter and span the barrier. Viscous forces must now incorporate both losses within the pool and the barrier. We find

$$h_{p \max} \sim \frac{2\sigma}{\Delta\rho g - Q\mu \left(\frac{f_b}{k_b A_b} + \frac{f_p}{k_p A_p} \right)} \left[\frac{1}{R_{nw}} - \frac{1}{R_{nwp}} \right], \quad (5)$$

where $h_{p \max}$ is defined as the distance from the far edge of the capillary barrier to the top of the pool, f is the fraction of $h_{p \max}$ that is within each unit, and subscripts b and p apply to the barrier and pool, respectively. Note that both f_b and f_p are a function of $h_{p \max}$, and thus (5) is not explicit in $h_{p \max}$ and requires iterative solution.

Because the R values in (5) are for different materials, both of which have sharp pressure saturation curves in our experi-

ment, (5) is not very sensitive to the value of the saturation that we use to take corresponding R . Neglecting viscous forces and taking R corresponding to an average S_{nw} of ~ 0.3 from the drainage curves in Figure 2 for the coarse to medium CB ($R_{nw} \sim 0.0085$ cm and $R_{nwp} \sim 0.0172$ cm), $h_{p \max}$ is ~ 8.7 cm for the CO_2 invasions. Comparison to a measured mean $h_{p \max}$ for CO_2 of ~ 7 cm shows the estimates based on the pressure-saturation curves to be high by $\sim 25\%$ of the measured value. There are at least four possible explanations for this discrepancy. The first is that the internal porous geometry of the units, especially that composing the CB, was different from that where the properties were measured. This is probable as the heterostructure and the homogeneous packs were filled and packed with different methods. The second is that the thickness of the CBs allowed them to breach at a lower pressure. All the CBs were thin, ~ 1 cm (~ 20 pores), and laterally extensive, $\sim 10 \times 1$ cm ($\sim 200 \times 20$ pores), and thus the probability of breaching the barrier at a lower pressure should be enhanced. The third is that our assumption of invariant contact angles for all fluid-fluid systems is incorrect, and thus the R distributions are different. Visual inspection of entrapped nonwetting phase, however, showed very little if any deviation from a contact angle of zero between the systems. Finally, it is possible that the higher pressures required to breach the CB material were capable of moving some grains of sand such as to create, on average, a larger set of pores spanning the barrier.

Since all of these possibilities work to modify the bracketed term in (5) primarily by increasing R_{nw} , we scale it to match the CO_2 data (factor of 1.1) yielding $h_{p \max}$ for TCE of ~ 5.7 cm without viscous forces. For the TCE injection, mean $h_{p \max}$ (only measurable before CB4) attained ~ 11 cm in the primary heterostructure. Taking measured values for k and Q , and estimating A within the pool to be ~ 6 cm², if we take $16\delta^2$ for the backbone of the conducting finger network within the barrier, (5) matches the measured value of ~ 11 cm for TCE. Similar calculations for the fine CB of the secondary heterostructure yield $h_{p \max}$ of ~ 20 cm neglecting viscous forces and ~ 40 cm including them. The distance between the fine CB and CB3 above is ~ 24 cm, and we see in the experiment that the pool comprises the full coarse structure between. Thus for both TCE experiments we again find that when viscous forces are important, the most critical data are the cross-sectional area within the backbones of the conducting finger network, here spanning the CB, and this value must once again be small and on the pore scale to match the pool height data.

Similar relations are easily written for the pool heights at which intermediate units are entered such as seen in our experiment within the secondary heterostructure. Additionally, while not explored in our experiments, we note that viscous forces will also influence pool geometry as units become wider by causing the breakthrough of capillary barriers before the entire pool unit is laterally spanned and filled to a uniform pool depth. For a 2-D pool such as we have in our experiment, we can approximate the horizontal expansion distance $h_{p \text{ hor}}$ by balancing ΔP_v for flow horizontal within the pool unit against the total pressure required for breaching the barrier to yield

$$h_{p \text{ hor}} \sim h_{p \max} (1 - f_b) \frac{\Delta\rho g k_p A_p}{Q\mu}, \quad (6)$$

where A_p now is an approximate average vertical cross-sectional area per unit thickness of the pool and $h_{p \max}$ is given by (5). For the coarse-medium transition and our flow rates, if we take A_p as $0.5 h_{p \max}$, we calculate an $h_{p \text{ hor}}$ of ~ 30 cm for

TCE and ~ 1.8 m for CO_2 , both wider than our system width. We can see the beginnings of horizontal viscous force influence in Plate 2b where more distant coarse regions fill at the same time as higher more central regions in the pool above CB4 (see yellow in image). We also note that if the nonwetting fluid can find a way around the CB within the horizontal distance $h_{p \text{ hor}}$, the CB will not be breached by a vertical finger.

4.4. Pulsation Within a Pool

When a finger spans a CB, it encounters a lower capillary pressure in the unit beyond. The pores within the CB and the pool behind thus can experience a depressurization. If their pressure decreases to the wetting entry values for pores in the pool or the CB, they will be reinvaded with the wetting fluid. For the pool, pores at the top of the pool will be reinvaded, and the pool height will drop. Additionally, smaller pores along the pool edges are also likely candidates for reentry. For the CB breached by fingers, the smallest pores which join the clusters of a finger are the most likely to be reinvaded with water.

To consider the reentry of pool pores with the wetting fluid after a CB is breached, we balance viscous forces across the pool/barrier system against capillary and gravity forces to yield $h_{t \text{ pool}}$:

$$h_{t \text{ pool}} \sim \frac{2\sigma}{\Delta\rho g - Q\mu \left(\frac{f_b}{k_p A_b} + \frac{f_p}{k_p A_p} \right)} \left[\frac{1}{R_{nw2}} - \frac{1}{R_{w1}} \right], \quad (7)$$

where subscripts 1 and 2 denote the unit before and beyond the CB, respectively. As with (5), (7) is not explicit in $h_{t \text{ pool}}$. Evaluation of this relation with values used previously yields $h_{t \text{ pool}}$ of ~ 4.2 cm for the CO_2 and of ~ 8.9 cm for TCE. Because the pool height (~ 7 cm) is greater than $h_{t \text{ pool}}$ for the CO_2 experiment, pores within the pool are immediately reinvaded with wetting fluid, and the pool height begins to drop as soon as the CB is spanned. For TCE the same should occur, but it does not. We believe that this difference is likely due to our simplified treatment of viscous forces within the barrier. If A_b is reduced from 16δ to 12δ , (7) matches the $h_{p \text{ max}}$ of ~ 11 cm. Thus the reinvasion of a small number of critical pores with water can increase the viscous drop across the barrier and yield an $h_{t \text{ pool}}$ the same as $h_{p \text{ max}}$ such that the pool height will not decrease until flow stops and redistribution begins. Such a small change in local saturation is likely within the noise of our imaging system and thus is very difficult to detect.

Pool height will decrease until the critical pore within the CB is reinvaded with the wetting fluid. For negligible viscous forces and assuming the influence of the growing finger below the CB is curtailed at the CB, this minimum pool height $h_{p \text{ min}}$ is given by

$$h_{p \text{ min}} \sim \frac{2\sigma}{\Delta\rho g} \left[\frac{1}{R_{wb}} - \frac{1}{R_{wp}} \right], \quad (8)$$

where subscripts b and p refer to the barrier and pool, respectively. Taking R_{wb} and R_{wp} as ~ 2 times their nonwetting values yields $h_{p \text{ min}}$ of $\sim 0.5 h_{p \text{ max}}$ or ~ 3.5 cm. Comparison to the CO_2 experiment where we find $h_{p \text{ min}}$ of ~ 3.0 cm shows (8) to fit our data reasonably well. Once the CB closes, h_p must once again achieve $h_{p \text{ max}}$ before it reopens thus causing the \sim factor of 2 unit-scale pool throbbing seen in the CO_2 invasion. The only pool that does not throb throughout the invasion period is behind CB1. There we see that the finger through the CB itself pulsates, something we do not detect in any of the

other CBs. This pulsation suggests a pathway through the barrier with large backbone pores which may be reinvaded at much lower pressures thus curtailing large excursions in pool height.

5. Basis of a “Structural” Growth Model for Nonwetting Phase Migration

The results of our experiments and analysis point to the critical pore-scale control of the invasion process. Incorporating such pore-scale control into standard porous continuum approaches is problematic. However, substructures within the heterogeneous experiments, including where pulsation will occur, can be reasonably well predicted with the set of length scales derived through scale analysis. We use this result as the foundation of a “structural” growth model for nonwetting phase migration within a heterogeneous aquifer. By structural growth model we mean a model that produces the evolution of nonwetting phase structure, the resulting finger and pool spatial configuration, and the zones where dynamic pulsation occurs. Considering first the situation where viscous forces are negligible, for a given heterogeneity structure with known pressure saturation curves for each unit, we can predict the growth of the nonwetting phase straightforwardly by assembling features defined by our scale analysis–derived length scales. The size of fingers, the height of pools, the penetration of CBs, and the regions where pulsation will occur can all be delineated from the point of injection to the boundaries of the field. With further knowledge of Q , the permeability for each unit, and relations for the critical conducting backbone areas for fingers both within and below CBs, nonnegligible viscous forces could then be included as a perturbation of the inviscid structure yielding increased pond heights and finger widths. Finally, if it is important at the scale of application, the influence of both pulsation and viscous forces to generate divergent pathways (i.e., multiple and divergent fingers) could be considered and superimposed on the core model results to yield the final nonwetting phase structure within the domain.

In order to develop confidence in such a structural growth model, our experiments suggest that we must understand in order of importance: (1) the interplay between capillary and gravity forces in context of interfacies and intrafacies lithologic variation, (2) the added influence of viscous forces, and (3) the possible additional complication imparted by pulsation. Obviously, facies-scale or macrolithologic variation controls the core structure of the nonwetting phase migration and thus is of highest importance. However, we also expect that the migration process will be affected by the ever present intrafacies microlayering found in subsurface sediments with the internal contrast and length scales (vertical and horizontal) of the sub-scale structure critically controlling nonwetting invasion just as we see in our current macroheterogeneous experiments. The importance of this structure will increase as both its contrast and length scales increase. In general, we expect greater meandering parallel to the microlayering (usually horizontal) within a given unit. While for wetting fluid advance such microlayering yields a wider macroscopic structure that may be consistent with unit-scale anisotropic effective properties, we are skeptical that a similar approach will be valid for nonwetting invasion. However, the greater horizontal meandering should cause a greater randomness within the invasion structure because a larger number of units can be sampled as invasion progresses.

When viscous forces are nonnegligible, prediction of finger diameter and pool height and width within a heterogeneous formation now requires knowledge of both Q and A_f composing the conducting backbone of the finger network that forms. It is likely that a relationship between Q and A_f will exist such as to only require knowledge of Q . Unfortunately, since A_f is not the total cross-sectional area occupied by a finger, the results of linear stability theory applied to continuum equations typically used to develop such a relation is insufficient. Therefore we must resort to a combination of experimentation and alternative analysis. Such an approach could use the work of Held and Illangasekare [1995a, 1995b] as a starting point.

Pulsation such as seen in our experiments has been found in rough-walled fractures for both wetting [Nicholl *et al.*, 1993; Glass and Nicholl, 1996] and nonwetting [Glass and Nicholl, 1995] gravity-driven invasion under imposed constant flux conditions. Because of its basic similarity to the dripping faucet dynamic, pulsation could be chaotic, as suggested for fractures by Nicholl *et al.* [1993]. Regardless of whether it is chaotic or periodic, pulsation will generate different nonwetting phase fluid pathways in time such as we see below CB4 in both the TCE and CO₂ experiments. Thus on a small scale we hypothesize pulsation to impart a rich spatial and temporal variability superimposed on the basic structural form selected by simple gravity and capillary forces within the heterogeneous field.

While the effects of viscous forces and pulsation are required to completely explain the migration behavior at small scale, will these added complexities matter for prediction of DNAPL migration at the field scale? The critical influences are not those that influence local saturations but are those that influence the large-scale pathway of DNAPL migration. Viscous forces will cause greater pool depths which can cause the selection of a pathway that spills over before the local CB is breached. However, viscous forces can also inhibit lateral migration over and around a CB and thus contribute to its breaching. These two influences will compete with each other, and so the combination may yield only a small influence in pathway choice; however, at present it is difficult to develop a generic rule of thumb for whether viscous forces contribute to lateral migration or inhibit it. Both viscous forces and pulsation also cause multiple finger formation and thus the possibility of divergent pathways. However, at the field scale this influence should be small unless the large-scale pathway is sensitive to small changes in connection via either multiple fingers or pulsation. Thus, while further research is required, we believe the aspects of multiple finger formation and pulsation to be of second or even third order with respect to prediction of nonwetting migration at the field scale.

Finally, we note that the "structural" growth model outlined above is simply a further upscaling of macro MIP models originally suggested by Glass *et al.* [1993] for the migration of DNAPL at the field scale. This approach has significant advantages over two-phase continuum models as it allows several orders of magnitude increased geological detail to be incorporated into the problem domain. As we have shown in our experiments, this detail critically controls the invasion structure. Unfortunately, at the majority of spill sites we may never know enough geological detail for deterministic modeling approaches to be more than marginally useful in finding DNAPLs. However, probabilistic modeling approaches, such as Monte Carlo analysis, show promise in aiding DNAPL source zone characterization efforts, and, fortunately, unlike two-phase continuum models, MIP models carry a light com-

putational burden and are thus well suited to Monte Carlo analysis. Borchers *et al.* [1997] showed that Monte Carlo simulation of DNAPL migration through three-dimensional (3-D) geological fields could be used to produce a probability map of potential DNAPL source zone location. In an example problem such simulation was used to create many realizations of plausible heterogeneous lithologies based on what was known about the system, while still reflecting the degree of remaining uncertainty. A MIP model was then used to simulate DNAPL migration on each realization, and the results of the ensemble were compiled into a probability map of where the DNAPL resides. Using such an approach, uncertainty about the distribution of geological features and the disposal history at the site can be propagated through the probabilistic modeling effort to reflect the degree of uncertainty in the extent of DNAPL migration. The probability map can then either be used directly or used in conjunction with decision tree approaches to suggest favorable sampling and/or recovery locations.

6. Concluding Remarks

Our experiments clearly demonstrate nonwetting invasion occurring as a sequence of gravity-stabilized and gravity-destabilized displacements within the heterogeneous media. Pore-scale gravity-destabilized fingers occur in all units as they are entered, but they are overwritten by macroscopic gravity-stabilized displacements behind capillary barriers that create backward growing macroscopic pools. The extent of the overwriting depends on the pool height before breakthrough of its controlling capillary barrier. This is illustrated in the secondary heterostructure, where similar gravity-driven fingering as seen in the primary heterostructure was completely overwritten in the top two thirds of the chamber. Such overwriting of fingers suggests that the destabilized signature of the flow will often be missed in experiments without capturing appropriate time history data, especially for experiments conducted in the field.

Our experiments show the majority of the mass is held in high-saturation regions commonly referred to as pools. A much smaller portion of the mass is held at residual saturation either in drained fingers or in the drained portion of pools. While this is not at all a startling revelation, we point out that experiments and analyses founded on an assumption of nonwetting phase held predominantly as a residual saturation may have limited applicability to situations where mass is held predominantly in pools. Failure to consider the presence of DNAPLs held in pools during remediation design may lead to decreased performance or inadvertent downward mobilization. For example, in designing a surfactant flood to enhance aqueous solubility, using the results of laboratory column studies or trapping number calculations based on the assumption of residual saturation may significantly underestimate the potential for mobilization of mass held in pools. On a more positive note we consider that the filling of pools provides the primary mechanism for lateral spreading and thereby the opportunity for detecting DNAPL source zones through the placement of vertical boreholes. This approach may prove profitable in cases where geological knowledge is sufficient to identify potential locations of lithologic traps and thus to hypothesize where the pools are likely to be. Indeed, explicitly identifying the locations of pools may provide the opportunity to pump organic liquids from them prior to attempting more exotic remediation strategies.

Our experiments also clearly show the existence of pulsation

behind the invasion front both at the pore scale within fingers and at the pool scale behind capillary barriers. This dynamic is due to the combination of gravitational forces and hysteretic capillary forces with viscous forces working to suppress pulsation as flow rate increases. To our knowledge this is the first time such dynamics have been clearly observed and explained. At present we expect pulsation to occur under most circumstances as long as viscous forces are "low enough." It is interesting to note that viscous fingering, which creates extreme randomness under conditions of high flow rate has, at low flow rate, a gravity/capillary controlled counterpart that also increases randomness in pathway formation. A more thorough understanding of the pulsation phenomena is required to fully consider this effect and its repercussions for predictability; however, we expect that for field-scale migration problems, its influence is minimal.

Comparison of scale analysis-derived length scales and experimental measurements show nonwetting invasion structure and dynamics to be controlled at the pore scale. The competition between local random capillary forces, gravity forces, and viscous forces acting along the narrow conducting backbone creates the dynamic that yields the stringed cluster structure of gravity-driven fingers. We find that this pore-scale finger structure can also control the pressure at which a capillary barrier breaches. Viscous forces acting along the conducting backbone of the fingers penetrating the capillary barrier can become significant and of the same order as capillary and gravity. Thus analyses of the importance of viscous forces for a particular problem must properly account for finger structure.

The results of our experimental work have implication for two-phase modeling approaches currently in use. Given the intrinsic pore-scale nature of finger formation and propagation, together with the local nature of the failure of capillary barriers, we question whether two-phase, porous continuum-scale modeling would be able to capture the unstable, lithology-driven migration behavior found in our experiments. To the extent that we believe our laboratory-constructed lithology provides a reasonable analogue to a field situation, we question the suitability of this class of models to field applications as well. Our experiments and those presented by *Glass and Nicholl* [1996] for gravity-destabilized wetting fluid invasion in heterogeneous systems also question the relevance of approaches based on stability analysis in homogeneous media to predict details such as finger width, the number of fingers, or finger velocity in heterogeneous media. In the field, heterogeneities and capillary barriers will focus flow into a series of "zones" or "points" rather than a distributed source such as analyzed through simple linear stability theory. While knowledge of system stability derived from such an analysis is important, quantitative predictions based on such an approach are highly speculative.

As an alternative, we propose a simplified approach based on our length-scale analysis as a more appropriate means to model nonwetting phase movement under many natural gradient conditions similar to our experiments. In principle, knowledge of the heterogeneous porous network structure and critical unit properties of saturated permeability and pressure-saturation curves allows us to predict the structure of the invasion pathway directly. Beginning with a core structure formed by capillary and gravity forces, and incorporating effects imposed by viscous forces or pulsation as needed, allows us to generate phase structure growth with a set of physically based rules. Such a structural growth model is a very different

approach to prediction than the standard two-phase continuum approach used by the vast majority of researchers and forms a class of upscaled MIP. However, implementation of upscaled MIP not only allows but requires sufficient geological detail at the scale controlling migration behavior, that is, the scale where significant textural contrasts occur. To the extent that deterministic data at that scale will seldom be available, we recommend probabilistic modeling of migration through multiple geological fields that capture the essence of the lithologic architecture.

Acknowledgments. This research was partially supported by Sandia National Laboratories Research and Development Program and the Department of Energy's Environmental Science Management Program and Basic Energy Science Geoscience Program under contract DE-AC04-94AL85000. John Gilletly helped conduct the experiments, and Erik Webb gave advice on the design of the heterogeneous sand pack. We thank Martin Blunt, Clinton Willson, and especially Toby Ewing for their constructive and helpful reviews of the manuscript.

References

- American Society for Testing and Materials, ASTM D 971-91, Standard test method for interfacial tension of oil against water by the ring method, in *Annual Book of American Society for Testing and Materials Standards*, vol. 10.03, pp. 119–121, Philadelphia, Pa., 1991.
- Anderson, M. R., R. L. Johnson, and J. F. Pankow, Dissolution of dense chlorinated solvents into groundwater, 3, Modeling contaminant plumes from fingers and pools of solvent, *Environ. Sci. Technol.*, 26(5), 901–908, 1992.
- Began, A., The method of scale analysis: Natural convection in fluids, in *Natural Convection, Fundamentals and Applications*, edited by S. Kakac, W. Aung, and P. Viskanta, pp. 75–94, Hemisphere Publishing, New York, 1985.
- Blunt, M. J., and H. Scher, Pore-level modeling of wetting, *Phys. Rev. E Stat. Phys. Plasmas Fluids Relat. Interdiscip. Top.*, 52:6-B, 6387–6403, 1995.
- Borchers, B., S. H. Conrad, E. K. Webb, R. J. Glass Jr., and R. Cox, A simulation and decision analysis approach to locating DNAPL in subsurface sediments, *Sandia Rep. SAND97-2261*, 22 pp. Sandia Natl. Lab., Albuquerque, N. M., 1997.
- Brewster, M. L., A. P. Annan, J. P. Greenhouse, B. H. Kueper, G. R. Olhoeft, J. D. Redman, and K. A. Sander, Observed migration of a controlled DNAPL release by geophysical methods, *Ground Water*, 33(6), 977–987, 1995.
- Conrad, S. H., J. L. Wilson, W. Mason, and W. Peplinski, Observing the transport and fate of petroleum hydrocarbons in soils and in groundwater using flow visualization techniques, paper presented at Symposium on Environmental Concerns in the Petroleum Industry, Am. Assoc. of Pet. Geol., Palm Springs, Calif., May 10, 1989.
- Ewing, R. P., and B. Berkowitz, A generalized model for simulating initial migration of dense non-aqueous phase liquids, *Water Resour. Res.*, 34, 611–622, 1998.
- Glass, R. J., and M. J. Nicholl, Near drift two-phase flow processes within regionally saturated fractured rock, paper presented at 6th International Conference of High Level Radiation Waste Management, Am. Nucl. Soc., Las Vegas, Nev., May 1–5, 1995.
- Glass, R. J., and M. J. Nicholl, Physics of gravity-driven fingering of immiscible fluids within porous media: An overview of current understanding and selected complicating factors, *Geoderma*, 70, 133–163, 1996.
- Glass, R. J., and L. Yarrington, Simulation of gravity-driven fingering in porous media using a modified invasion percolation model, *Geoderma*, 70, 231–252, 1996.
- Glass, R. J., J.-Y. Parlange, and T. S. Steenhuis, Wetting front instability, 1, Theoretical discussion and dimensional analysis, *Water Resour. Res.*, 25, 1187–1194, 1989a.
- Glass, R. J., T. S. Steenhuis, and J.-Y. Parlange, Wetting front instability, 2, Experimental determination of relationships between system parameters and two-dimensional unstable flow field behavior in initially dry porous media, *Water Resour. Res.*, 25, 1195–1207, 1989b.
- Glass, R. J., T. S. Steenhuis, and J.-Y. Parlange, Mechanism for finger

- persistence in homogeneous unsaturated porous media: Theory and verification, *Soil Sci.*, 148, 60–70, 1989c.
- Glass, R. J., S. H. Conrad, and E. K. Webb, Percolation approaches to modeling immiscible fluid movement in subsurface systems (abstract), *Eos Trans. AGU*, 74(43), Fall Meet. Suppl., 278, 1993.
- Glass, R. J., E. K. Webb, and S. H. Conrad, An upscaled buoyant invasion percolation model for use in approaches to delineate subsurface DNAPL location, *AIChE Symp. Ser.*, 306(91), 23–29, 1995.
- Held, R. J., and T. H. Illangasekare, Fingering of dense nonaqueous phase liquids in porous media, 1, Experimental investigation, *Water Resour. Res.*, 31, 1213–1222, 1995a.
- Held, R. J., and T. H. Illangasekare, Fingering of dense nonaqueous phase liquids in porous media, 2, Analysis and classification, *Water Resour. Res.*, 31, 1223–1232, 1995b.
- Illangasekare, T. H., J. L. Ramsey Jr., K. H. Jensen, and M. B. Butts, Experimental study of movement and distribution of dense organic contaminants in heterogeneous aquifers, *J. Contam. Hydrol.*, 20, 1–25, 1995.
- Illangasekare, T. H., J. E. Ewing, and K. O. Pytte, Process upscaling of nonaqueous phase liquid behavior in heterogeneous aquifers, Paper presented at Specialty Conference on Non-aqueous Phase Liquids (NAPLs) in Subsurface Environment: Assessment and Remediation, Am. Soc. of Civ. Eng., Reston, Va., Washington, D. C., Nov. 12–14, 1996.
- Ioannidis, M. A., I. Chatzis, and F. A. L. Dullien, Macroscopic percolation model of immiscible displacement: Effects of buoyancy and spatial structure, *Water Resour. Res.*, 32, 3297–3310, 1996.
- Ji, W., A. Dahmani, D. P. Ahlfeld, J. D. Lin, and E. Hill III, Laboratory study of air sparging: Air flow visualization, *Ground Water Monit. Rem.*, 13(4), 115–126, 1993.
- Kueper, B. H., and D. B. McWhorter, The use of macroscopic percolation theory to construct large-scale capillary pressure curves, *Water Resour. Res.*, 28, 2425–2436, 1992.
- Kueper, B. H., W. Abbot, and G. Farquhar, Experimental observations of multiphase flow in heterogeneous porous media, *J. Contam. Hydrol.*, 5, 83–95, 1989.
- Kueper, B. H., D. Redman, R. C. Starr, S. Reitsma, and M. Mah, A field experiment to study the behavior of tetrachloroethylene below the water table: Spatial distribution of residual and pooled DNAPL, *Ground Water*, 31(5), 756–766, 1993.
- Lenormand, R., and C. Zarcone, Invasion percolation in an etched network: Measurement of a fractal dimension, *Phys. Rev. Lett.*, 54, 2226–2229, 1985.
- Nicholl, M. J., R. J. Glass, and H. A. Nguyen, Small-scale behavior of single gravity driven fingers in an initially dry fracture, in *Proceedings of 4th International Conference of High Level Radiation Waste Management*, pp. 2023–2033, Am. Nucl. Soc., Lagrange Park, Ill., 1993.
- Norton, D. L., Evaluation, extension and application of a full field light transmission technique for the investigation of hysteresis in thin homogeneous sand slabs, Ph.D. dissertation, Univ. of Ariz., Tucson, 1995.
- Powers, S. E., I. M. Nambi, and G. W. Curry Jr., Non-aqueous phase liquid dissolution in heterogeneous systems: Mechanisms and local equilibrium modeling approach, *Water Resour. Res.*, 34, 3293–3302, 1998.
- Stanley, H. E., Cluster shapes at the percolation threshold: An effective cluster dimensionality and its connection with critical point exponents, *J. Phys. A Math. Gen.*, 10, L211, 1977.
- Stauffer, D., and A. Aharony, *Introduction to Percolation Theory*, 2nd ed., Taylor and Francis, Philadelphia, Pa., 1992.
- Tidwell, V. C., and R. J. Glass, X-ray and visible light transmission for laboratory measurement of two-dimensional saturation fields in thin slab systems, *Water Resour. Res.*, 30, 2873–2882, 1994.
- Weast, R. C. (Ed.), *CRC Handbook of Chemistry and Physics*, 66th ed., CRC Press, Boca Raton, Fla., 1985.
- Wilson, J. L., S. H. Conrad, W. R. Mason, W. Peplinski, and E. Hagan, Laboratory investigation of residual liquid organics from spills, leaks, and the disposal of hazardous wastes in groundwater, *Rep. EPA/600/6-90/004*, Environ. Prot. Agency, Washington, D. C., 1990.
- S. H. Conrad, R. J. Glass, and W. Peplinski, Flow Visualization and Processes Laboratory, Sandia National Laboratories, Albuquerque, NM 87185. (shconra@sandia.gov; rjglass@sandia.gov; wjpepli@sandia.gov)

(Received August 20, 1999; revised January 17, 2000; accepted May 15, 2000.)

